

Ferromagnetism and spin-dependent transport at a complex oxide interface

Yilikal Ayino¹, Peng Xu², Juan Tigre-Lazo¹, Jin Yue², Bharat Jalan², and Vlad S. Pribiag^{1*}

¹ *School of Physics and Astronomy, University of Minnesota, Minneapolis, MN 55455, USA*

² *Department of Chemical Engineering and Materials Science, University of Minnesota, Minneapolis, MN 55455, USA*

The interface between complex oxides can host a high-mobility conducting electron gas, even though the constituent materials are insulators. Since the initial discovery of this phenomenon in LaAlO₃/SrTiO₃ (LAO/STO) heterostructures [1], several other materials systems with this property have been identified [2-4]. These systems host a range of highly-correlated phases, including superconductivity [5,6] and ferromagnetism [7-12]. While superconductivity has been conclusively detected using transport [5,6,8,13] and scanning-probe measurements [9], reports of magnetism have been more difficult to reconcile across experiments. Magneto-transport studies [7,14] have reported pronounced magnetic hysteresis, suggestive of stable ferromagnetic order, however scanning-probe magnetometry [9] and neutron scattering [15] studies have generally detected low magnetic moments. Here, we report ferromagnetism at the NdTiO₃/SrTiO₃ (NTO/STO) interface, and show that electronic transport is mediated by spin-dependent hopping between localized magnetic regions which become superparamagnetic above ~1.5 K. The electronic properties of the NTO/STO heterostructures do not originate from oxygen vacancies, dislocations or substrate defects [16,17]. This suggests that these factors are not responsible for the observed magnetic properties.

To date, the microscopic details and the physical origin of magnetism in complex oxide interfaces remain elusive [15,18,19]. A tantalizing possibility is that spin ordering emerges from electronic reconstruction at these interfaces [20,21]. Driven by this prospect, numerous studies have investigated the magnetic properties of the canonical LAO/STO [7-9] system. However, a unified picture of ferromagnetism in LAO/STO is still lacking [7-9,15,22]. A major challenge stems from the possible role of sample-specific disorder, such as oxygen vacancies, dislocations and roughness [23-25]. Since LAO/STO is typically grown by pulsed-laser deposition (PLD) of LAO onto STO substrates, both stoichiometry and epitaxy near the interface have been difficult to control precisely [26]. Moreover, the STO substrate is typically an integral part of the interface. This poses an additional challenge since STO substrates contain defects which include unintentional magnetic impurities [27]. Therefore, in order to shed light on the possible intrinsic nature of interfacial magnetism, it is crucial to mitigate the role of disorder and magnetic impurities. To achieve this we study NTO/STO heterostructures, which are grown using hybrid molecular beam epitaxy (hMBE). hMBE is an ultra-high vacuum MBE technique recently developed for the growth of complex oxides [28]. Importantly, both NTO and STO are grown using hMBE, which ensures the highest possible control over stoichiometry at the interface [4,16,17]. Moreover, the LSAT substrate does not play any direct role in the properties of the interface.

Here, we investigate the magnetic properties of hMBE-grown NTO/STO using electronic transport meas-

urements at temperatures down to 150 mK. Bulk NTO is a Mott-Hubbard anti-ferromagnetic insulator with Mott-Hubbard gap of 0.8 eV and Néel temperature of ~90 K [29], while STO is a band insulator with a gap of 3.2 eV. Similar to the case of LAO/STO, electronic reconstruction at the NTO/STO interface forms a high-density quasi-two-dimensional electron gas (2DEG) [17]. Band structure calculations and x-ray measurements show that the 2DEG resides on the STO side of the NTO/STO interface [17]. The carrier concentration of stoichiometric NTO/STO heterostructures with less than 6 unit cells of NTO is 0.5 electrons per unit cell (u.c.) of STO ($3.2 \times 10^{14} \text{ cm}^{-2}$) [17], in excellent agreement with the prediction of the polar discontinuity model for polar-non-polar oxide interfaces [1]. Interestingly, electron densities typically reported for LAO/STO samples are an order of magnitude lower than this predicted value. While the exact reason for this discrepancy in LAO/STO has not yet been resolved [16,30] this suggests that charged defects do not play an important role in our NTO/STO interfaces. Here we focus on a stoichiometric sample (sample A) with layer thicknesses STO (40 u.c.) / NTO (4 u.c.) / (La_{0.3}Sr_{0.7})(Al_{0.65}Ta_{0.35})O₃ (LSAT) (001) (substrate).

The temperature-dependence of the sheet resistance, R_s , is shown in Fig. 1a for different values of the magnetic field, B , applied in the plane of the sample. R_s follows an Arrhenius-law behavior, $R_s \propto \exp[\frac{\varepsilon}{k_B T}]$, consistent with thermally-activated electronic transport, where k_B is the Boltzmann constant, T is the temperature and ε is the activation energy. Remarkably, ε decreases by over 60% of its $B=0$ value when a 6 T field is applied.

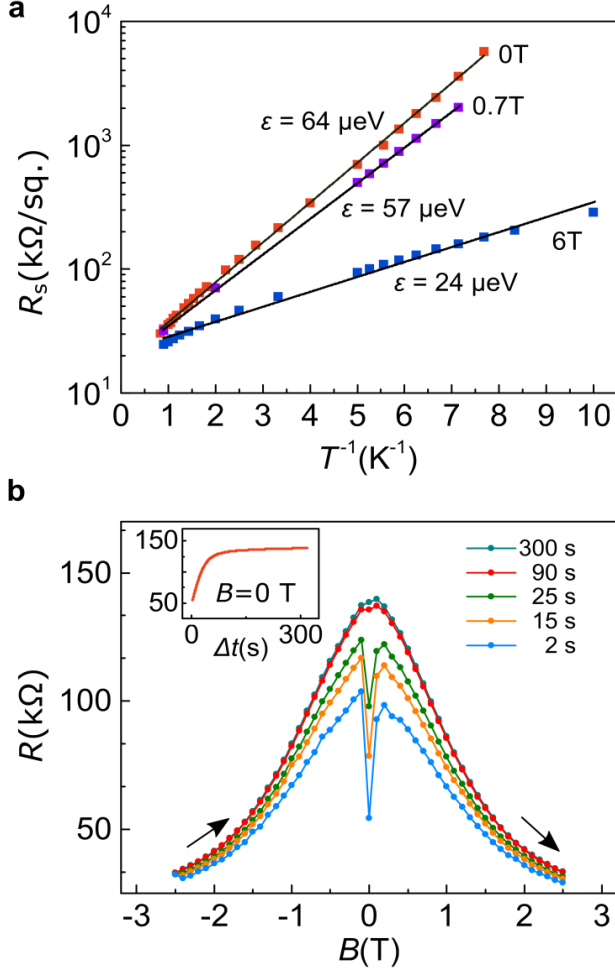


Fig. 1: Sheet resistance and magnetoresistance. a, Sheet resistance as a function of inverse temperature for three different values of B . Lines correspond to fits to $\exp[-\frac{\epsilon}{k_B T}]$. The data show a weak deviation from a simple Arrhenius law at larger values of B , which indicates that ϵ acquires a small temperature-dependence as B increases. b, Resistance as a function of magnetic field at different values of Δt . Inset: resistance as a function of Δt for $B = 0$ T.

This indicates that magnetic effects dominate transport through the sample at low temperatures.

To further investigate the magnetic properties of the sample we measure the resistance, R , as a function of B , while also recording its time-dependence. Specifically, we step the value of B , then record R as a function of Δt , the time elapsed since setting B to its current value (a full two-dimensional plot of R vs. B and Δt is shown in Supplementary Figure S1). Fig. 1b shows the magnetoresistance for several values of Δt . Two main features stand out. First, R decreases by up to $\sim 75\%$ of its zero-field value upon application of a 2.5 T field. Second, curves

measured at small Δt exhibit a sharp resistance dip near $B=0$, which gradually decreases with increasing Δt and eventually disappears for $\Delta t > \sim 90$ s. The inset of Fig. 1b shows the time-evolution of R at a fixed value of B . Initially, R increases rapidly from a value of ~ 55 k Ω , then saturates around a stable value of ~ 140 k Ω , with a characteristic evolution time $\Delta t^* \sim 25$ s. We focus first on the steady-state properties ($\Delta t \gg \Delta t^*$), then return to the significance of the transient dip.

Magneto-transport in the steady-state

Important information about the underlying transport mechanism is obtained from the temperature evolution of the magneto-resistance ($MR \equiv \frac{R(B)-R(0)}{R(0)} \times 100\%$). At low temperatures, R becomes strongly suppressed for large B , yielding a large negative MR of up to -95% for $B = 6$ T at 150 mK (see Fig. 2a). As T is increased from 150 mK, the MR curves become gradually shallower and eventually acquire a slightly positive curvature for $T > \sim 4$ K. In contrast to the large and strongly temperature-dependent negative MR observed below 4 K, the MR does not exceed $\sim 0.2\%$ and is only weakly temperature-dependent above 4 K. This suggests that distinct processes dominate transport above and below 4 K.

Large negative MR has been observed in LAO/STO [7,31,32], leading to several possible explanations, including ferromagnetic ordering [7], the Kondo effect [32,33], and a non-interacting model based on strong spin-orbit coupling [31]. Although these models capture key features of the data, a quantitative description is still missing. Below, we propose a simple model which accounts for all features of our data with high accuracy. The decrease in activation energy ϵ with increasing B (Fig. 1a) is reminiscent of carrier delocalization under applied magnetic field reported in mixed-valence manganites, which show colossal magnetoresistance [34,35]. In those materials electrons are localized by a spin-dependent potential barrier, but become delocalized by an applied magnetic field. In our samples, the magnetic field dependence of R is largely independent of the direction between B and the sample (Supplementary Fig. S2), consistent with spin-dependent effects. Despite the differences between NTO/STO and manganites, the activation energy, ϵ , can be separated on general grounds into a spin-independent contribution, ϵ_0 , and spin-dependent contribution, ϵ_s , yielding $\epsilon = \epsilon_0 + \epsilon_s$. The spin-dependent energy cost for hopping from site 1 to site 2, with magnetization unit vectors \mathbf{M}_1 and \mathbf{M}_2 respectively, can be written as $\epsilon_{12}^s = -\alpha \mathbf{M}_1 \cdot \mathbf{M}_2$, where α characterizes the hopping energy [35]. Macroscopic averaging leads to $\epsilon_s = -\alpha(M/M_s)^2$, where M is the magnetization and M_s the saturation magnetization of the sample.

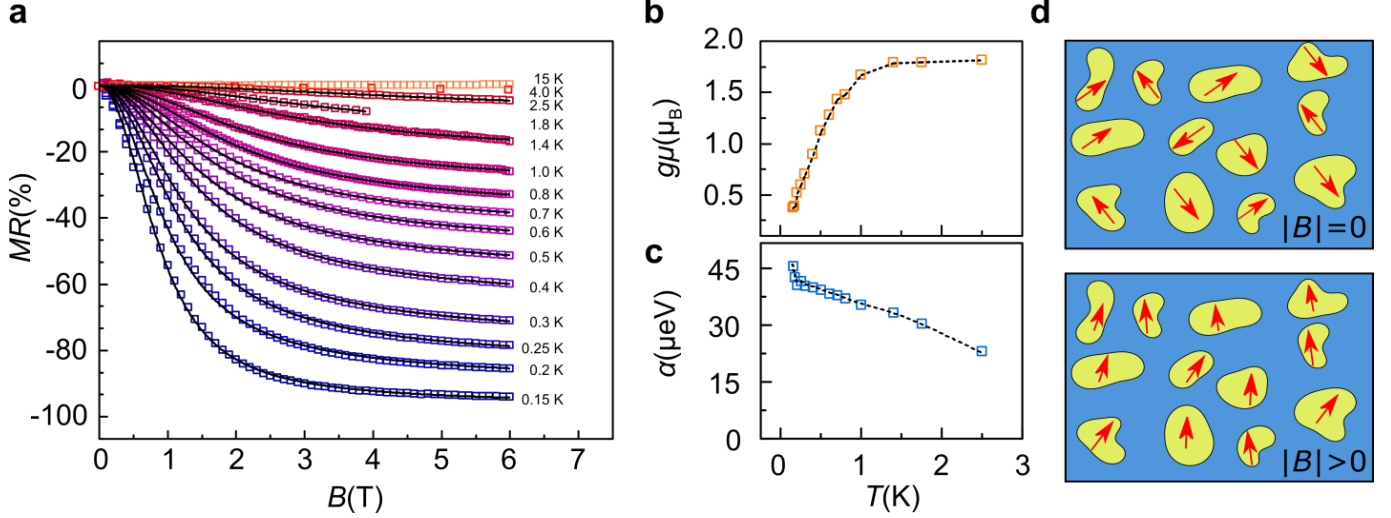


Fig. 2: Magnetoresistance ratio and model fits. a, Magnetoresistance ratio at different values of T . Solid lines are fits to eqn. (1) for $T < \sim 4\text{K}$, where a pronounced negative MR is observed. b, Temperature evolution of the average fluctuating moment, μ , multiplied by the effective g -factor, displayed in units of Bohr magnetons. Values are obtained from the fits in a. c, Temperature evolution of the fitting parameter α . The gradual decrease in α with increasing temperature could be due to gradual loss of spin coherence during hopping at larger temperatures. The dotted black lines in b & c are guides to the eye. d, Schematic showing the net moments of the superparamagnetic islands discussed in the main text. The upper panel shows randomly oriented magnetic regions at $B = 0$, while the lower panel depicts the moments becoming polarized for finite values of B .

In the paramagnetic limit, where M vanishes for $B=0$, the MR can therefore be expressed as:

$$MR = \left(\text{Exp} \left[- \frac{\alpha}{k_B T} \left(\frac{M}{M_s} \right)^2 \right] - 1 \right) \times 100\% \quad (1)$$

For paramagnetic and superparamagnetic systems the local moments fluctuate and the average value of the M is described by the Brillouin function, B_j , where j is the angular momentum of each fluctuating moment. For larger values of j , fluctuating moments behave classically and the Brillouin function quickly approaches the Langevin function, yielding $\frac{\langle M \rangle}{M_s} = L(g\mu B/k_B T)$, where g is the effective Landé g -factor and μ is the magnitude of the average fluctuating moment. To test the validity of our model, we fit equation (1) to the MR data (Fig. 2a). We find an excellent agreement over more than one order of magnitude in temperature using only two fitting parameters, α and $g\mu$. Interestingly, the Brillouin expression for the quantum paramagnet does not yield good fits for small $j < \sim 10\hbar$ when $T > \sim 1.5\text{K}$. This indicates that the angular momentum of each local moment is larger than $\sim 10\hbar$, which justifies using the classical description.

The remarkable fit of the model to the negative MR data suggests a simple microscopic picture in which electrons undergo spin-dependent hopping between magnetic regions for $T < 4\text{K}$ (Fig. 2d). The moments of these re-

gions fluctuate over time as described by the Langevin function. The lower bound on j discussed above points to the magnetic regions being clusters with local ferromagnetic order, rather than individual atomic sites. Thus, μ is a measure of the average moment of the magnetic clusters that are fluctuating at a given temperature. Consistent with this picture, the values of $g\mu$ extracted from the fit are approximately constant for $T > 1.5\text{K}$ (Fig. 2b). This indicates that for $1.5\text{K} < T < 4\text{K}$ all magnetic regions undergo large-amplitude superparamagnetic fluctuations. On the other hand, for $T < 1.5\text{K}$, $g\mu$ decreases rapidly and approaches zero near $T=0$. This suggests that below 1.5K the regions with larger μ cease to fluctuate because $k_B T$ decreases below their magnetic anisotropy energy. Since the smaller regions have smaller anisotropy energy they continue to fluctuate as the temperature is decreased, until they are also gradually blocked at lower T . Thus, 1.5K corresponds to an effective superparamagnetic blocking temperature of the entire sample.

Below $\sim 800\text{mK}$ the MR curves become hysteretic (Fig. 3), indicating that a large fraction of the superparamagnetic domains have been cooled below their blocking temperature. In this temperature range, magnetic anisotropy energies dominate over thermal effects. This stabilizes the direction of the local domains and leads to irreversible behavior. Consistent with this picture, the hysteresis becomes more pronounced with decreasing temperature (Fig. 3). The presence of hysteresis provides direct

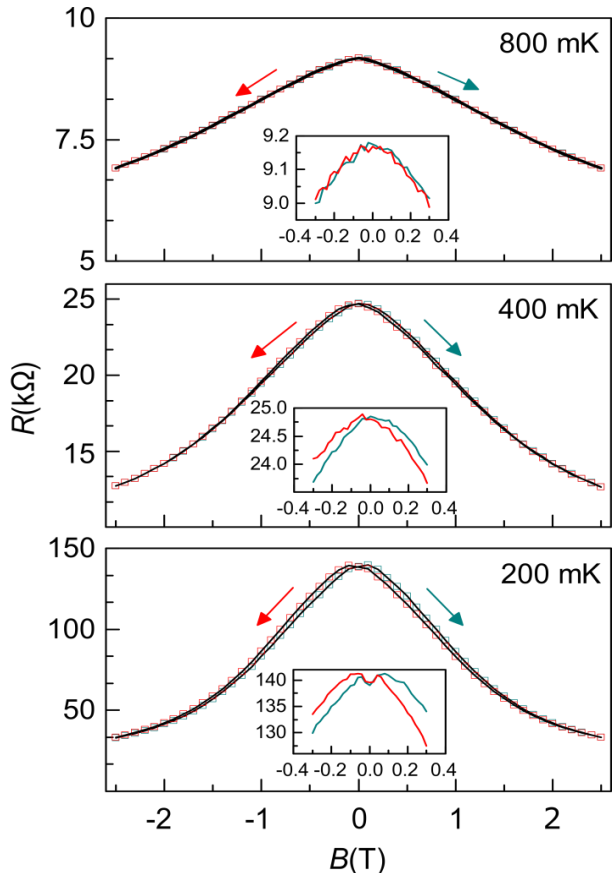


Fig. 3: Magnetoresistance hysteresis. R vs. B while stepping B from negative to positive value (cyan) and positive to negative values (red). The black lines are guides to the eye. Arrows indicate the direction along which B is stepped. Different panels correspond to different temperatures. Insets in each panel show a zoom-in near $B=0$, highlighting that hysteresis becomes more pronounced at lower T .

evidence for ferromagnetic ordering. We note that hysteresis is a sufficient, but not necessary signature of local ferromagnetism. Its presence only indicates that at low T the moments of the magnetic clusters do not fluctuate over the duration of the measurement.

Magneto-transport in the transient regime

We now turn to discussing the magnetoresistance measured at short delays, $\Delta t < \Delta t^*$. Fig. 4a shows the MR measured at $\Delta t = 2$ s and $T=200$ mK (bottom panel). The data shows a striking hysteric dip for $|B| < \sim 50$ mT. Such butterfly-shaped dips in the magneto-resistance have been previously used as evidence of interfacial magnetism in oxide interfaces and oxide thin films.[7,10,14] To investigate the origin of this effect, we performed a control experiment on a non-magnetic, Si-doped, insulating GaAs crystal with similar resistance to that of sample A (Fig.

4b). Strikingly, the MR curve measured on GaAs at $\Delta t = 2$ s shows a similar hysteric butterfly-shaped dip (Fig. 4b, bottom panel) as the NTO/STO sample. This feature is also transient, as shown in Fig. 4b, upper panel, measured for $\Delta t = 320$ s. Since the GaAs sample is a high-purity non-magnetic bulk crystal, this demonstrates that this transient hysteric resistance dip is not the result of magnetism in the sample, but is instead an extrinsic effect. This conclusion is further supported by a similar measurement on a BaSnO_3 thin film (Supplementary Fig. S4).

Having ruled out intrinsic magnetism as the origin of the transient hysteresis, we now consider the possibility of a magneto-thermal origin. Interestingly, of all the samples we studied, the transient dip was observed only in semi-insulating samples, for which R has a large upturn at low T (e.g. Fig. 1a and inset of Fig. 4c). In contrast, metallic samples, for which R is only weakly temperature dependent at low T , show no transient hysteresis. This is consistent with a magneto-thermal origin of the transient hysteresis dip, which is likely extrinsic to the sample itself: for semi-insulating samples even a small increase in the effective sample temperature leads to a substantial decrease in R .

To quantify this effect, we extracted the effective temperature of our STO/NTO/LSAT sample as a function of B at $\Delta t = 2$ s (Fig. 4c) (see Supplementary Figure S3 for details). We find that the transient hysteric effect is associated with an increase in sample temperature by only ~ 30 mK, which develops as B is stepped through the -80 mT to $+80$ mT range. This rapid increase in temperature near $B=0$ could be due to heat released by an avalanche magnetic reversal process. Such processes are commonly observed when the spin configuration of a ferromagnet, spin glass or spin-ice switches abruptly [36]. The presence of such a magneto-thermal material nearby our sample is confirmed by the fact that the mixing chamber temperature of our dilution refrigerator rises by ~ 5 mK as B crosses zero. While we cannot precisely determine the location of the magneto-thermal material, we note that magneto-thermal effects are common and can have dramatic consequences [37] below several Kelvin, where the relative change in T can be large. The hysteric nature of the butterfly-shaped resistance dip can be understood as a consequence of the characteristic thermal re-equilibration time of the sample, which we estimate to be $\sim \Delta t^* \sim 25$ s (Fig. 1b and Supplementary Figure S1).

In conclusion, we observe ferromagnetic ordering at the epitaxial interface between NTO and STO. We find that ferromagnetism develops inhomogeneously in isolated regions, which are superparamagnetic at temperatures between 1.5 K and 4 K. Electronic transport is in excellent agreement with spin-dependent, thermally-activated

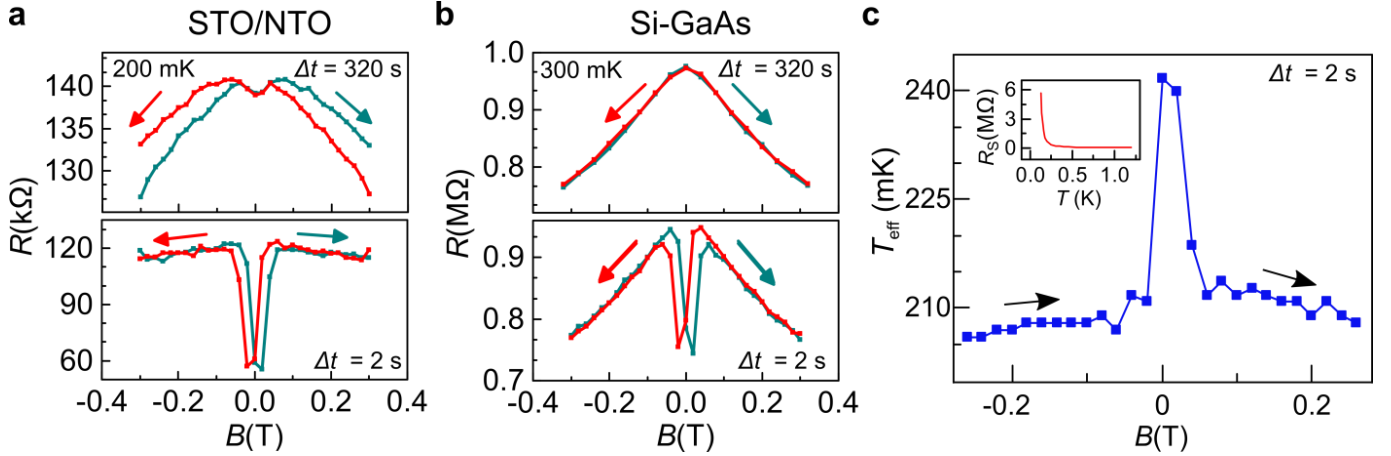


Fig. 4: Magnetoresistance at short Δt . R vs. B for: a, sample A, with composition STO(40 uc)/NTO(4 uc)/LSAT, and b, for a Si-GaAs control sample. For both samples, a hysteretic dip develops near $B = 0$ at short Δt (lower panels), while no such dip is observed at long Δt (upper panels). Unlike the NTO/STO sample, the GaAs sample does not show any hysteresis in the steady state, but only a weak, reversible, negative MR , consistent with quantum interference effects in insulating n-GaAs[38]. c, Extracted effective temperature of sample A as a function of B for $\Delta t = 2$ s. The arrows indicate the direction along which B is stepped. Inset: R vs. T for sample A, showing the steep dependence of R with T at low values of T , characteristic of semi-insulating behavior.

hopping between the ferromagnetic regions. Furthermore, we highlight the importance of time-dependent measurements for distinguishing signatures of magnetic order from extrinsic magneto-thermal effects. The observed magnetism is unlikely to originate from oxygen vacancies, dislocation defects or substrate impurities, since these factors are not responsible for the electronic properties of our NTO/STO heterostructures [16,17]. Thus, the inhomogeneous magnetic phase observed here could be due in part to electronic reconstruction. However, interfacial roughness likely also plays an important role. This is supported by the fact that large negative MR ratios are observed only in heterostructures where STO was grown on NTO, but not in samples where the growth order was reversed (Supplementary Figure S5). The layer order is significant because atomic resolution electron microscopy shows the former interfaces to be rough on the atomic scale due to intermixing, while the latter are atomically sharp [17]. Further experiments can benefit from using nanoscale devices to probe transport over the length scales of individual magnetic regions and to assess the potential for oxide-interface spintronic devices.

Methods: Samples were grown using hMBE, as described in Ref. [17]. Measurements were performed in a four-terminal van der Pauw configuration, in a dilution refrigerator equipped with three-axis vector rotate magnet, with a base temperature of 15 mK. Due to the thermally-activated nature of transport in our samples, the current-voltage (I - V) characteristics become nonlinear for $T \lesssim 150$ mK, indicating non-Ohmic transport (see Sup-

plementary Figure S6). We therefore focused on $T \geq 150$ mK. Samples were contacted by wire-bonding to sputtered Al (40nm)/Ni(20nm)/Au(300nm) contacts. We studied in detail four stoichiometric samples with layer structures STO(t u.c.)/NTO(4 u.c.)/LSAT, where t was varied between 8 and 40 u.c. All samples had resistances in the range of 100 - 1000 k Ω and showed large negative MR . Persistent hysteresis was observed only in sample A, discussed in the main text. The lack of detectable hysteresis for $\Delta t \gg \Delta t^*$ in the other samples indicates very low magnetic coercivities in those samples. This further suggests that the irreversible contributions to ferromagnetic reversal are sensitive to sample-specific disorder, likely interfacial roughness.

Acknowledgements: The authors thank E. D. Dahlberg, J. Levy, A. Morpurgo and B. Shklovskii for valuable discussions. This work was supported primarily by the National Science Foundation (NSF) Materials Research Science and Engineering Center (MRSEC) at the University of Minnesota Under Award Number DMR-1420013, and through the Young Investigator Program of the Air Force Office of Scientific Research (AFOSR) through Grant FA9550-16-1-0205. Device fabrication was performed in part at the Minnesota Nano Center (MNC), which is partially supported by the NSF through the National Nanotechnology Coordinated Infrastructure (NNCI).

Author contributions: Y.A. and V.S.P. performed the measurements. Y.A., P.X., J.T.-L., J. Y., B.J and V.S.P. analyzed the data. P.X. and B.J. prepared the samples.

Y.A. and V.S.P. wrote the manuscript. V.S.P. planned and supervised the project. All authors contributed to editing the manuscript.

* vpribiag@umn.edu

- [1] A. Ohtomo and H. Y. Hwang, *Nature* **427**, 423 (2004).
- [2] P. Moetakef *et al.*, *Appl. Phys. Lett.* **99**, 232116, 232116 (2011).
- [3] M. Takizawa *et al.*, *Phys. Rev. Lett.* **97**, 057601, 057601 (2006).
- [4] P. Xu, D. Phelan, J. S. Jeong, K. A. Mkhoyan, and B. Jalan, *Appl. Phys. Lett.* **104**, 082109 (2014).
- [5] N. Reyren *et al.*, *Science* **317**, 1196 (2007).
- [6] J. Biscaras, N. Bergeal, A. Kushwaha, T. Wolf, A. Rastogi, R. C. Budhani, and J. Lesueur, *Nat. Commun.* **1**, 89 (2010).
- [7] A. Brinkman *et al.*, *Nat. Mater.* **6**, 493 (2007).
- [8] L. Li, C. Richter, J. Mannhart, and R. C. Ashoori, *Nat. Phys.* **7**, 762 (2011).
- [9] J. A. Bert, B. Kalisky, C. Bell, M. Kim, Y. Hikita, H. Y. Hwang, and K. A. Moler, *Nat. Phys.* **7**, 767 (2011).
- [10] P. Moetakef, J. R. Williams, D. G. Ouellette, A. P. Kajdos, D. Goldhaber-Gordon, S. J. Allen, and S. Stemmer, *Phys. Rev. X* **2**, 021014, 021014 (2012).
- [11] D. Stornaiuolo *et al.*, *Nat. Mater.* **15**, 278 (2016).
- [12] Y. Anahory *et al.*, *Nat. Commun.* **7**, 12566 (2016).
- [13] A. D. Caviglia *et al.*, *Nature* **456**, 624 (2008).
- [14] D. A. Dikin, M. Mehta, C. W. Bark, C. M. Folkman, C. B. Eom, and V. Chandrasekhar, *Phys. Rev. Lett.* **107**, 056802, 056802 (2011).
- [15] M. R. Fitzsimmons *et al.*, *Phys. Rev. Lett.* **107** (2011).
- [16] P. Xu, Y. Ayino, C. Cheng, V. S. Pribiag, R. B. Comes, P. V. Sushko, S. A. Chambers, and B. Jalan, *Phys. Rev. Lett.* **117**, 106803, 106803 (2016).
- [17] P. Xu, T. C. Droubay, J. S. Jeong, K. A. Mkhoyan, P. V. Sushko, S. A. Chambers, and B. Jalan, *Adv. Mater. Interfaces* **3**, 1500432 (2016).
- [18] S. Banerjee, O. Erten, and M. Randeria, *Nat. Phys.* **9**, 625 (2013).
- [19] Z. Salman *et al.*, *Phys. Rev. Lett.* **109**, 257207, 257207 (2012).
- [20] R. Pentcheva and W. E. Pickett, *Phys. Rev. B* **74**, 035112, 035112 (2006).
- [21] S. Okamoto, A. J. Millis, and N. A. Spaldin, *Phys. Rev. Lett.* **97**, 056802, 056802 (2006).
- [22] M. Salluzzo *et al.*, *Phys. Rev. Lett.* **111**, 087204 (2013).
- [23] I. S. Elfimov, S. Yunoki, and G. A. Sawatzky, *Phys. Rev. Lett.* **89**, 216403, 216403 (2002).
- [24] N. Pavlenko, T. Kopp, E. Y. Tsymbal, G. A. Sawatzky, and J. Mannhart, *Phys. Rev. B* **85**, 020407, 020407 (2012).
- [25] B. Kalisky, J. A. Bert, B. B. Klopfer, C. Bell, H. K. Sato, M. Hosoda, Y. Hikita, H. Y. Hwang, and K. A. Moler, *Nat. Commun.* **3**, 922, 922 (2012).
- [26] M. P. Warusawithana *et al.*, *Nat. Commun.* **4**, 2351 (2013).
- [27] J. M. D. Coey, M. Venkatesan, and P. Stamenov, *J. Phys.: Condens. Matter* **28**, 485001, 485001 (2016).
- [28] B. Jalan, P. Moetakef, and S. Stemmer, *Appl. Phys. Lett.* **95**, 032906 (2009).
- [29] A. S. Sefat, J. E. Greedan, and L. Cranswick, *Phys. Rev. B* **74**, 104418, 104418 (2006).
- [30] W. Siemons, G. Koster, H. Yamamoto, W. A. Harrison, G. Lucovsky, T. H. Geballe, D. H. A. Blank, and M. R. Beasley, *Phys. Rev. Lett.* **98**, 196802 (2007).
- [31] M. Diez, A. Monteiro, G. Mattoni, E. Cobanera, T. Hyart, E. Mulazimoglu, N. Bovenzi, C. W. J. Beenakker, and A. D. Caviglia, *Phys. Rev. Lett.* **115**, 016803, 016803 (2015).
- [32] J. Ruhman, A. Joshua, S. Ilani, and E. Altman, *Phys. Rev. B* **90**, 125123, 125123 (2014).
- [33] A. Joshua, J. Ruhman, S. Pecker, E. Altman, and S. Ilani, *PNAS* **110**, 9633 (2013).
- [34] J. M. D. Coey, M. Viret, L. Ranno, and K. Ounadjela, *Phys. Rev. Lett.* **75**, 3910 (1995).
- [35] P. Wagner, I. Gordon, L. Trappeniers, J. Vanacken, F. Herlach, V. V. Moshchalkov, and Y. Bruynseraede, *Phys. Rev. Lett.* **81**, 3980 (1998).
- [36] D. Slobinsky, C. Castelnovo, R. A. Borzi, A. S. Gibbs, A. P. Mackenzie, R. Moessner, and S. A. Grigera, *Phys. Rev. Lett.* **105**, 267205, 267205 (2010).
- [37] A. J. Bestwick, E. J. Fox, X. F. Kou, L. Pan, K. L. Wang, and D. Goldhaber-Gordon, *Phys. Rev. Lett.* **114**, 187201, 187201 (2015).
- [38] F. Tremblay, M. Pepper, R. Newbury, D. Ritchie, D. C. Peacock, J. E. F. Frost, G. A. C. Jones, and G. Hill, *Phys. Rev. B* **40**, 10052 (1989).

Supplementary Information

Ferromagnetism and spin-dependent transport at a complex oxide interface

Yilikal Ayino¹, Peng Xu², Juan Tigre-Lazo¹, Jin Yue², Bharat Jalan², and Vlad S. Pribiag^{1*}

¹ *School of Physics and Astronomy, University of Minnesota, Minneapolis, MN 55455, USA*

² *Department of Chemical Engineering and Materials Science, University of Minnesota, Minneapolis, MN 55455, USA*

List of supplementary figures:

Supplementary Fig. S1: Time-dependent magnetoresistance data

Supplementary Fig. S2: Angular dependence of resistance

Supplementary Fig. S3: Estimation of sample temperature due to extrinsic magneto-thermal heating

Supplementary Fig. S4: Magnetoresistance of a BaSnO₃ control sample.

Supplementary Fig. S5: Magnetoresistance of a NTO/STO/LSAT sample (reversed growth sequence with respect to sample A, discussed in the main text).

Supplementary Fig. S6: Voltage vs. current curves vs. T for sample A.

Procedure for the time-dependent magnetoresistance measurements:

The time-dependent MR is measured using the following procedure. Before starting the measurement B is first set at some large negative or positive value. During the measurement, B is stepped and held constant while the resistance is measured as a function of time delay Δt under constant B . The field is stepped again after when Δt reaches 320 s, then the procedure is repeated. All measurements are performed under constant current bias. This procedure generates a three-dimensional data set: R as a function of B and Δt (Fig. S1). This is represented in the 2D color plot with magnetic field and delay in each axis and resistance represented by a color scheme, Fig S1 (a). It can also be represented in 1D plot of resistance as a function of the total time elapsed since the beginning of the measurement S1 (b).

The timescale for the suppression of the butterfly-shaped hysteretic dip (Fig. 1b and Supplementary Figure S1) suggests a characteristic timescale for temperature re-equilibration of $\sim \Delta t^* \sim 25$ s. This highlights the importance of analyzing the time-dependence of the MR when investigating signatures of magnetism in oxide interfaces or other materials for which the resistance is strongly temperature-dependent at low temperatures.

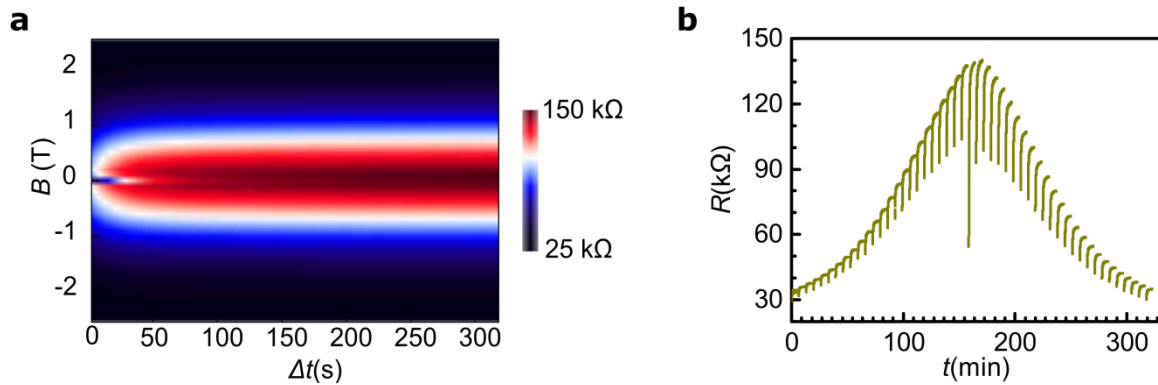


Fig. S1: Time-dependent magnetoresistance data. **a**, Two-dimensional color plot of R as a function of B and Δt . **b**, One-dimensional plot of the time-evolution of R plotted vs. the total time elapsed from the beginning of the measurement. Each curve represents resistance measured at a B . B is stepped during the time intervals which separate the curves, at which point the resistance is not measured.

Angular dependence of resistance:

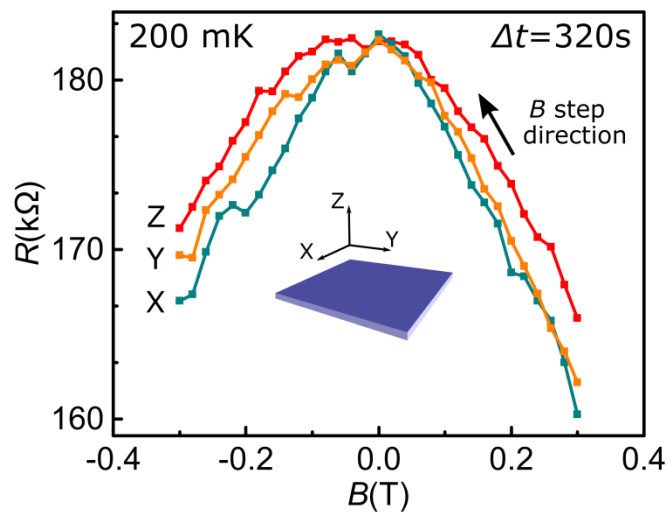


Fig. S2: Angular dependence of resistance. The resistance is largely independent of the direction of the applied field B with respect to the sample plane. The MR is slightly smaller when B is applied out of plane (along Z) than in the plane (along X or Y). This is consistent with a weak in-plane magnetic anisotropy.

Estimation of sample temperature due to extrinsic magneto-thermal heating:

As discussed in the main text, the resistance of the sample is a strong function of T , B and Δt . In order to determine the effective sample temperature (T_{eff}) at a given B and Δt we use the steady-state MR curves taken at $\Delta t \gg \Delta t^*$ as reference. Specifically, we assume that for $\Delta t \gg \Delta t^*$, $T_{\text{eff}} = T_{\text{mix}}$, where T_{mix} is the mixing chamber temperature. To acquire the calibration data, we measure R as a function of B and Δt for T_{mix} ranging from 200 mK to 270 mK in 5 mK increments. At each temperature, we ensure that T_{mix} has stabilized near the desired setpoint before measuring R . The resulting steady-state data $R(\Delta t=320 \text{ s}, T_{\text{mix}}, B)$ are shown in Fig. S2.

To determine T_{eff} as a function of B in the transient regime ($\Delta t < \Delta t^*$) when T_{mix} is set to 200 mK, we compare the measured values of $R(\Delta t, T_{\text{mix}}=200 \text{ mK}, B)$ with the steady-state calibration data, $R(\Delta t=320 \text{ s}, T_{\text{mix}}, B)$. This provides an estimate of T_{eff} at short delay for $T_{\text{mix}}=200 \text{ mK}$ at each value of B . Because of the finite resolution of T_{mix} increments (5 mK), we use spline interpolation to estimate temperatures from resistance values which fall in between adjacent points. Hence the uncertainty of T_{eff} is estimated to be $\pm 2.5 \text{ mK}$.

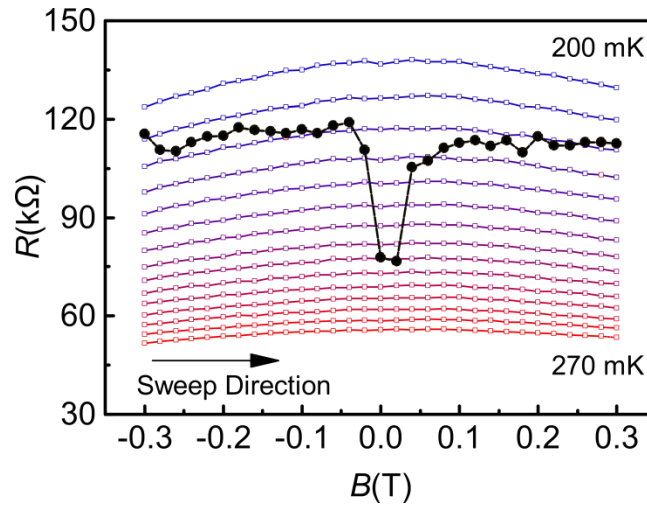


Fig. S3: Estimation of sample temperature due to extrinsic magneto-thermal heating. Curves with open points represent long delay resistance, $R(\Delta t=320 \text{ s}, T_{\text{mix}}, B)$, for T_{mix} ranging from 200 mK to 270 mK in 5 mK increments. The overlaid curve with solid points is the short delay data, $R(\Delta t = 2 \text{ s}, T_{\text{mix}}=200 \text{ mK}, B)$, showing that near zero field a temperature spike of approximately 30-40 mK occurs for $T_{\text{mix}} = 200 \text{ mK}$.

Magnetoresistance of a BaSnO₃ control sample:

In addition to the Si-GaAs control sample discussed in Fig. 4 of the main text, we also performed a similar control experiment on a semi-insulating BaSnO₃ thin film. We found the same behavior: a hysteretic butterfly-shaped dip appears at low Δt and vanishes in the steady-state, for $\Delta t > \sim 200$ s (Fig. S4). The only samples which did not show a transient butterfly-shaped dip were metallic (NTO/STO) samples for which the resistance is a weak function of temperature at low temperatures. This is consistent with a heating origin of the resistance dip, as discussed in the main text.

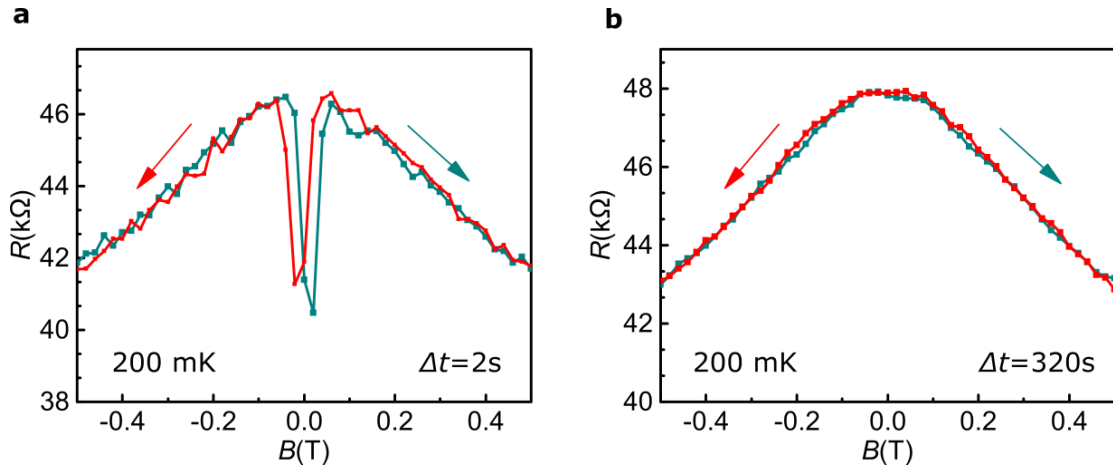


Fig. S4: Magnetoresistance of a BaSnO₃ control sample. **a**, R as a function of B at short delay ($\Delta t = 2$ s) for control sample thin film consisting of a La-doped BaSnO₃ (BSO) thin film (layer structure is La-BSO(100nm)/BSO(120 nm)/STO (substrate)). The resistance shows a hysteretic dip near zero field, similar to that seen for STO/NTO/LSAT samples, as discussed in the main text. **b**, Resistance as function of magnetic field at ($\Delta t = 320$ s), showing that the dip disappears in the steady state.

NTO/STO/LSAT sample (inverted layer sequence with respect to sample A in main text):

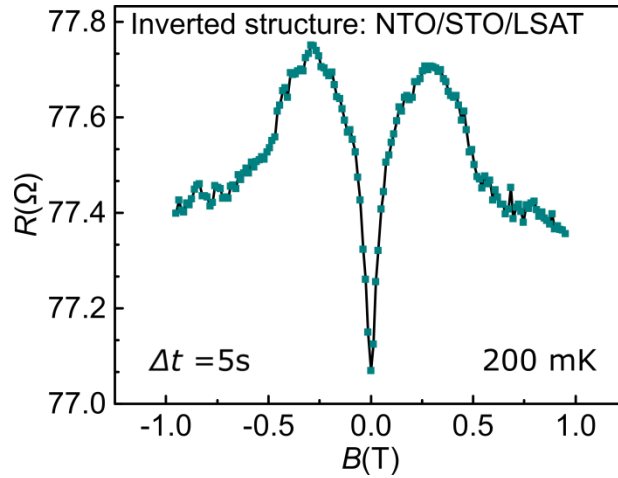


Fig. S5: Magnetoresistance of a NTO/STO/LSAT sample (reversed growth sequence with respect to sample A, discussed in the main text). R vs. B for a NTO(20 u.c.)/STO(24 u.c)/LSAT heterostructure. Note that the NTO layer grown on the STO layer, which is opposite to the order for sample A, which is discussed in the main text. The data shows a small sharp positive MR near $B=0$. Away from $|B| > \sim 0.3$ T there is a small decrease in resistance. The absence of large negative MR is characteristic of heterostructures grown with such “inverted” layer ordering, which have an atomically-sharp interface.

Voltage vs. current curves at low temperatures:

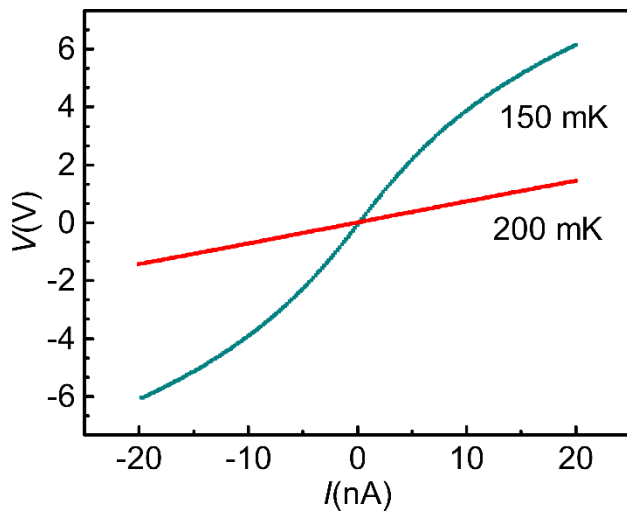


Fig. S6: Voltage vs. current curves vs. T for sample A. Voltage drop (V) across the sample as a function of applied bias current (I) for $T=150$ mK and $T=250$ mK. For $T = 150$ mK the V - I curve becomes nonlinear for $I > \sim 3$ nA. For this reason, the data in the main text was taken at $T \geq 150$ mK.